

# Switching based Spin Transfer Torque Oscillator with zero-bias field and large tuning-ratio

*Gaurav Gupta<sup>1†</sup>, Zhifeng Zhu<sup>1</sup> and Gengchiao Liang<sup>1\*</sup>*

<sup>1</sup>Department of Electrical and Computer Engineering, National University of Singapore,  
Singapore 117576

We propose a novel concept of obtaining oscillations with frequencies in very-high frequency (VHF) and ultra-high frequency (UHF) bands. A traditional spin torque nano-oscillator (STNO) has one or a set of pinned layers (PL) and one or more a set of locked free layers (FL) which precesses in a fixed orbit, defined by a precession angle, which results in magneto-resistance (MR) oscillations. In STNO, with aligned or even orthogonal easy-axis of the magnetic layers and with or without external bias magnetic field, it is not possible to attain full MR swing which limits the extracted output power. Furthermore, the orbit is strongly afflicted with thermal fluctuations or magnetic noise. In stark contrast to the operation principle of STNO, we theoretically show, with the simulation parameters extracted from the experimental papers, that with a unidirectional current in a dual asymmetric free-layers (with no pinned layer) based perpendicular magnetic tunnel junction (pMTJ) both the free layers can attain complete and out-of-phase self-sustained switching without the aid of any external field. This design enables full MR swing, and hence larger output power, for stable and more thermally robust free-running oscillations. Furthermore, the integration with the n-type metal-oxide-semiconductor field-effect transistors (NMOS) at 130, 65 and 14 nm node is appraised to expound its effect on the oscillator performance, controllability with dc bias and the design constraints, to demonstrate the viability of the design as a dynamically controllable oscillator for practical on-chip implementation.

## I. INTRODUCTION

On-chip oscillators [1] generate stable periodic oscillations, whose voltage (VCO), current (CCO) or digital (DCO) control serves as an integral component of the phase-locked loop (PLL) and radio-frequency (RF) transceivers. PLL generates the clock signal for the chip serving as its heart, where it can either output the same or multiply or divide the VCO frequency to suit the application. Frequency ( $f$ ) control of the oscillators enables dynamic-frequency-scaling (DFS) scheme [2] for optimizing the low-power modes. Furthermore, as the indispensable blocks in RF transceiver circuits, oscillators are used for modulation and clock recovery. For these applications, an ideal oscillator needs large quality factor ( $Q$ ) (i.e. small phase noise), low power consumption ( $P_{IN}$ ), large output power or voltage swing ( $P_O$  or  $V_O$ ), integrability with CMOS, large tunability ratio ( $f_{max}/f_{min}$ ) and small die area occupancy in the desired frequency regime. Extant solutions [1, 3] are based on the ring-oscillators, which have low  $Q$ , for sub-GHz and LC-tank oscillators (large  $Q$ ) for a few GHz range, because phase noise for the ring oscillators further degrades as the frequency is scaled-up. Furthermore, LC oscillators have small tuning range [1, 4], have large  $P_{IN}$ , are difficult to integrate in the very-large scale integration (VLSI) chips and occupy large area because of the large inductor and varactor size even in low GHz regime at which custom-designed chips can operate.

To overcome these issues, recently spin-torque nano-oscillators (STNOs) and spin-hall nano-oscillators (SHNO) have been proposed [5] and integrated with CMOS [6]. They are expected to consume small area ( $\sim$  area of magnetic-tunnel junction (MTJ)), less power and provide ultra-wide-band operation [7, 8]. STNOs are based on the precession of a free-layer (or set of locked [9-11] FLs) of MTJ in a fixed orbit determined by the precessional angle [5], with a single or a set of fixed reference/pinned layer [12]. This precession in a locked orbit results in an oscillatory change in the magnetization of the free layer (s) with respect to

that of the reference layer, which translates into a resistance change of a MTJ (or spin-valve in case of metallic spacer),  $R_{\text{MTJ}}$  and thus an output voltage swing. To increase the output voltage swing by increasing the observable fraction of the MR in the oscillations, the combination of multiple in-plane and perpendicular magnetization free and pinned/reference layers (orthogonal set of layers [10, 13]) in a MTJ has also been promulgated for a very large precession angle. It enables near full rotation of one of the free layers, without external bias magnetic-field  $H_{\text{Applied}}$ , as an improvement over an all in-plane or all-perpendicular designs which need  $H_{\text{Applied}}$ . However, the use of orthogonal layers across the spacer (metal like Cu or insulator like MgO) inherently limits the MR of these stacks. Furthermore recently, locked precessional orbits of dual free layer designs, without polarizing layer, for in-plane magnetization (ii-MTJ) and with assistance of  $H_{\text{Applied}}$  have also been shown to produce stable oscillatory output [14, 15]. Without  $H_{\text{Applied}}$ , the output signal has been shown to be very weak ( $< -100$  dBm) [16]. Moreover, for multiple precessional orbits with the MR and the resistance oscillations depending on the dynamic angle of the precessions, the effect of the magnetic noise becomes stronger in this design compared to traditional STNO. Furthermore, sophisticated designs with tilted anisotropy, operating without  $H_{\text{Applied}}$ , with weak output ( $< -65$  dBm) [17], and more recently with large  $P_{\text{O}}$  (nearly  $-26$  dBm at 6.7mA current bias) which need very precise control of  $H_{\text{Applied}}$  and especially designed microstructure for the magnet [18, 19] in sombrero-shaped MTJ, have been demonstrated. As a consequence of the reliance on the fixed precessional orbit, the magnetic noise resulting from the thermal fluctuations strongly affects the performance of a STNO (for instance see Fig. 1 of Ref. [20] or Fig. 5 of Ref. [21]), by randomizing the phase of the precession. This especially becomes pernicious when MTJ area is down-scaled because the thermal field scales as an inverse root of the magnet volume. These issues greatly limit its applicability in the real applications [7].

Therefore, in this work we propose a simple design of a spintronic oscillator, with no exotic structure or tilted anisotropy constraints, as conceptually illustrated in Fig. 1. The generated oscillations (85-1002 MHz) are in VHF and UHF frequency bands which more generally serve application-specific integrated circuits (ASICs) [2, 22-26], where VHF and UHF are the frequency bands defined by IEEE (Institute of Electrical and Electronics Engineers) standard as 30-300 MHz and 300-1000 MHz respectively. Furthermore, this frequency range also serves the RF band for LoRa protocol (868 MHz for Europe, 915 MHz for North America and 430 MHz for Asia) [27-29] which is deployed for low-cost bi-directional secure low-power wide-area-network (LPWAN) wireless communication channel in internet-of-things (IoT), machine-to-machine (M2M), smart city and industrial applications [30]. This is in contrast to STNO which is normally over this range and gets to tens of GHz and thus applied as microwave source/detector and in wireless transceivers [5, 7] for other protocols like Bluetooth and Wi-Fi. The proposed design is based on dual asymmetric free-layers, with no pinned layer, in a perpendicular magnetic tunnel junction (pMTJ) and operates without any bias magnetic field. The design has large tunability ratio and can deliver relatively large output power because MR oscillations attain full theoretical maximum, which in turn would also be much larger than MTJs with magnetic layers with orthogonal easy-axis. To achieve this, the design deploys a different operation principle than STNO. It is based on the switching of both the free-layers with unidirectional current in pMTJ structure, where one of the free-layer would have traditionally served as a reference layer and mandated current reversal for switching-back the traditional free-layer. It is shown that both layers can attain complete and out-of-phase self-sustained switching with a dc electrical bias to produce oscillations which are more thermally robust than for STNO.

The frequency is shown to scale directly with the MTJ current  $I_{\text{MTJ}}$ . In CCO configuration, the design has tunability of over a decade. This is much superior to STNO [31]

and ring oscillators [32] for which even attaining an octave (electronic control for STNO) is a challenge, and thus proposed design is better suited for DFS schemes. Since, CCO would warrant implementation of the stable current sources/mirrors over a wide operating range, which would heavily penalize the design in terms of power and area, simply driving the MTJ with a NMOS in VCO configuration is also appraised. Therefore, as illustrated in Fig. 2(a), the impact of integration and the control of the oscillator via foundry calibrated NMOS is also examined across the complementary metal–oxide–semiconductor (CMOS) nodes (130, 65 and 14 nm) by tuning either the gate voltage  $V_{GS}$  (suggested method in this work) or the node voltage  $V_{DD}$  (akin to the ring oscillator based VCOs) of the cell, where cell is referred to a system of a MTJ with a (or set of) driving NMOS. It is shown that transistor has significant impact on the performance metrics of the oscillator. The performance in general degrades, yet is shown to be better than traditional STNOs in the CCO configuration. Furthermore, we show that the NMOS area dominates the cell-size instead of the MTJ area, and hence should be the one compared with the traditional ring or LC oscillators to claim area benefits. Moreover, a larger node because of its larger supply voltage has better current drive and thus an iso-frequency comparison exhibits smaller channel area and larger output power for a larger node.

The article is organized as follows. In Sec. II, the methodology of our theoretical simulation of the proposed design is explained. Sec. III discusses the results and is anatomized into three sub-sections. In sub-section III.A, the operation principle and the device physics is expounded, the effect of thermal fluctuation i.e. magnetic noise is considered in III.B. Results for the design driven by a current-source thus operating it in CCO configuration is presented in III.C, while integration of transistors to operate in VCO configuration is assayed in III.D. This is followed in Sec. IV with the summary and conclusions of our study.

## II. METHODOLOGY

The simulation framework illustrated in Fig. 2(b) expounds the usage of tools in this work, variable exchange across the tools and their flow across the framework. Two methods are considered in this work to drive unidirectional current through a pMTJ based proposed oscillator. First is via constant current source (akin to suggested for STNO) which operates the device in the CCO configuration (Fig. 1), and corresponds to only the Matlab blocks in the framework. Second is via NMOS with MTJ on the drain end of the transistor whose supply node  $V_{DD}$  (akin to ring-oscillators) or gate (suggested method for this design) is controlled via input dc voltage, which operates the design in the VCO configuration (Fig. 2(a)). This invokes the full framework shown in Fig. 2(b).

Other configurations, like MTJ on the source end or use of the MOS in the diode mode results in inferior performance of the oscillator and thus not shown here. The voltage-dependent MTJ resistance is coded in verilog-A. The output and transfer characteristics of the high performance NMOS are extracted from the following experimental data from major foundries presented in IEDM (IEEE International Electron Device Meeting) over the years: 130 nm node bulk-NMOS data from Fig.4 and Fig. 6 of Intel transistors published in Ref. [33], 65 nm node bulk-NMOS data from Fig. 6 and Fig. 7 of IBM, Chartered and Infineon transistors published in Ref. [34], while 14 nm node FinFET (Fin Field Effect Transistor) from Fig. 5 and Fig. 6 of Intel transistors published in Ref. [35]. The channel area for 130 nm and 65 nm is computed as product of channel-length times channel-width, while for 14 nm FinFET its gate length times fin pitch times number of fins ( $n$ ), where  $n$  is an integer not less than the real number obtained by dividing effective channel-width by fin-width (fin-width = 2 fin-height + fin-thickness). The predictive technology files (PTM) available from University of California Berkley (UCB) have been optimized to fit the transistor characteristics. The transistors are modelled via open-source BSIM4 verilog-A code from Silvaco for bulk-

NMOS and from UCB for FinFETs. The circuit is simulated via SPICE solver SMASH 6.5.0 from Dolphin Solutions. The fitting (red line) of NMOS output characteristics via spice simulation against the extracted data (black circles) is shown for instance in Fig. 2(c) for 130 nm node, Fig. 2(d) for 65 nm node and Fig. 2(e) for 14 nm node. The magnetization dynamics is solved in Matlab via coupled Landau–Lifshitz–Gilbert (LLG) equation, integrated via fourth order Runge-Kutta method [36], for two FLs with macrospin model which has been shown to be valid for dimensions considered in this work [37-39]. The problem is numerically solved in matlab which is dynamically coupled with SMASH to solve at every time-interval  $\Delta t$  of 5 ps for updated angle between the two magnetization vectors and the voltage across the MTJ. Unless stated otherwise, the oscillator characteristics are extracted for 10  $\mu$ s run which results in two-million sampling points of the data which is subsequently parsed by Fast-Fourier Transform (FFT) to extract oscillator characteristics like fundamental frequency, linewidth, quality factor and output voltage swing  $V_O$ . The output power  $P_O$  in dBm is computed as  $10 + 20 \log_{10}(V_O)$ . Conceptually,  $V_O$  is half of the peak-to-peak voltage swing  $V_{PK-PK}$ . For input-power  $P_{IN}$  and area, in CCO configuration only MTJ is considered (akin to the STNO literature) while in VCO configuration both MTJ and transistor are accounted. Next, the Resistance-Area product or  $RA = 4.7 \Omega\text{-}\mu\text{m}^2$  is taken from CoFeB pMTJ from imec [40] with zero-bias TMR (Tunnelling Magnetoresistance) i.e.  $TMR_0 = 143\%$  and MgO thickness  $t_{MgO} = 1$  nm. Throughout the text, MTJ dimensions (in nm) along x, y and z axis are respectively expressed as: length  $\times$  width  $\times$  thickness<sub>FL1</sub> (thickness<sub>FL2</sub>), with default value of 50nm $\times$ 50nm $\times$ 1.6nm(1.2nm). Both damping and field-like torque (DLT and FLT),  $a_{\parallel}$  and  $a_{\perp}$  respectively, are considered in the coupled LLG equation as [41],

$$\left( \frac{1 + \alpha^2}{\gamma} \right) \frac{d\mathbf{M}_i}{dt} = -\mathbf{M}_i \times \left[ \mathbf{B}_{\text{Eff}}^i - (a_{\perp}^i + \alpha a_{\parallel}^i) \mathbf{p}_j \right] - \frac{\mathbf{M}_i}{M_S} \times \left\{ \mathbf{M}_i \times \left[ \alpha \mathbf{B}_{\text{Eff}}^i - (\alpha a_{\perp}^i - a_{\parallel}^i) \mathbf{p}_j \right] \right\} \quad (1)$$

where,  $\alpha = 0.01$  [41] is the damping constant,  $\gamma$  is the gyromagnetic ratio,  $i = 1$  and  $2$  denotes FL<sub>1</sub> and FL<sub>2</sub> respectively,  $\mathbf{M}_i$  is the magnetization vector of the  $i^{\text{th}}$  FL,  $\mathbf{p}_j$  is the unit-vector of the spin-angular momentum acting on the magnetic moments of the  $i^{\text{th}}$  FL due to  $j^{\text{th}}$  FL, where  $i \neq j$ . Hence,  $\mathbf{p}_j$  for FL<sub>2</sub> dynamics is parallel to  $\mathbf{M}_1$ , while for FL<sub>1</sub> dynamics its anti-parallel to  $\mathbf{M}_2$ .  $M_S = 1.2573 \times 10^6$  A/m [42] is the saturation magnetization of CoFeB based FL,  $\mathbf{B}_{\text{Eff}}^i$  is the effective magnetic field acting on  $i^{\text{th}}$  layer obtained as (superscript  $i$  is implied, wherever applicable, in all equations below),

$$\mathbf{B}_{\text{Eff}} = \mathbf{B}_{\text{Applied}} + \mathbf{B}_{\mathbf{K}} + \mathbf{B}_{\text{Dipole}} - \mathbf{B}_{\text{Demag}} + \mathbf{B}_{\mathbf{T}} \quad (2)$$

where,  $\mathbf{B}_{\text{Applied}}$  is a external bias magnetic field and set to zero vector in this work,  $\mathbf{B}_{\mathbf{K}}$  is uniaxial crystalline anisotropy field obtained as,

$$\mathbf{B}_{\mathbf{K}} = \frac{2}{M_S} \left( K_{\text{Bulk}} + \frac{K_{\text{Interface}}}{t_{\text{FL}}} \right) [0 \quad 0 \quad m_z]^T \quad (3)$$

where, magnetization unit vector  $\mathbf{m} = [m_x \quad m_y \quad m_z]$ ,  $K_{\text{Bulk}} = 2.245 \times 10^5$  J-m<sup>-3</sup> and  $K_{\text{Interface}} = 1.286 \times 10^{-3}$  J-m<sup>-2</sup> [42] is bulk and interface anisotropy constant,  $t_{\text{FL}}$  is the free-layer thickness in meter,  $\mathbf{B}_{\text{Dipole}}^i$  is the dipolar field acting on  $i^{\text{th}}$  layer due to presence of  $j^{\text{th}}$  layer and expressed as,

$$\mathbf{B}_{\text{Dipole}}^i = \mu_0 M_S \begin{bmatrix} D_{xx} & D_{xy} & D_{xz} \\ D_{yx} & D_{yy} & D_{yz} \\ D_{zx} & D_{zy} & D_{zz} \end{bmatrix} \begin{bmatrix} m_x^j \\ m_y^j \\ m_z^j \end{bmatrix} \quad (4)$$

where,  $\mathbf{D}$  is the 3×3 dipolar-tensor matrix and is calculated directly via analytical expressions from Ref. [43, 44].  $\mathbf{B}_{\text{Demag}}$  is the self-demagnetizing field of the FL, whose vector is expressed as,

$$\mathbf{B}_{\text{Demag}} = \mu_0 M_S [N_x m_x \quad N_y m_y \quad N_z m_z]^T \quad (5)$$

where,  $N_x$ ,  $N_y$  and  $N_z$  is computed via expressions in Ref. [45]. The thermal fluctuation field which induces magnetic noise in both the FLs is computed as [38, 46],

$$\mathbf{B}_T = \sqrt{\frac{2\alpha K_B T}{(1+\alpha^2)\gamma M_S \text{Vol}_{\text{FL}} \Delta t}} \left[ R_{0,1}^x \ R_{0,1}^y \ R_{0,1}^z \right] \quad (6)$$

where,  $K_B$  is the Boltzmann constant,  $\text{Vol}_{\text{FL}}$  is the volume of the FL. Along x, y and z-axis, independent random numbers  $R_{0,1}$  have Gaussian distribution of zero mean and unit standard deviation. We account for the thermal fluctuation field at every time-step. Here, we note that the current induced self-heating effects [47-49] have not been included in this work. For high quality MgO MTJs, which lack metallic pinholes in the tunnel junction either due to fabrication process or small cross-section of the MTJ [50], it was experimentally proven [51, 52] that joule heating is not the underlying mechanism for the dielectric breakdown, instead it is the strong electric field larger than 2V/nm across MgO insulator [51] that results in dielectric breakdown. Since, in this work we ensure that field is weaker than 1V/nm and picked high-quality pMTJ [40], we have ignored these secondary effects in our analysis in this work. We, however, note that in case joule heating dominates or is substantial enough to affect the oscillator characteristics, characteristics should in general degrade because of the increase in the magnetic noise and the slight degradation in the spin-polarization of the carriers [53]. Next, MTJ resistance  $R_{\text{MTJ}}$  calculation accounts for the voltage dependence of the TMR and the dynamic angle  $\theta$  between the two precessing FLs as,

$$R_{\text{MTJ}} = R_p + \frac{R_{\text{AP0}} - R_p}{1 + \frac{V_{\text{MTJ}}^2}{V_{\text{Half}}^2}} \left( \frac{1 - \cos(\theta)}{2} \right) \quad (7)$$

where,  $V_{\text{Half}} = 0.4$  V, extracted for CoFeB from Ref. [54], is voltage across MTJ at which TMR becomes half of its value at zero-bias i.e.  $\text{TMR}_0/2$ ,  $R_p$  is the MTJ resistance when both magnets are exactly parallel to each other and remains invariant to  $V_{\text{MTJ}}$  for all practical purpose [55, 56], while  $R_{\text{AP0}}$  is MTJ resistance when both magnets are exactly anti-parallel to each other at zero-bias. A pessimistic value of spin-polarization  $P$ ,  $P_1 = P_2 = 0.4$  [57, 58], of the spin-flux for both FLs is assumed to obtain conservative estimates of the oscillator

performance. The higher values of  $P$ , for instance from 0.5 to 0.8 [53, 57, 58], would proportionally scale down the MTJ current required to obtain the same oscillator frequency. Next, in the recent years Slonczewski expression [59, 60] for spin-torque efficiency  $\eta$  has been extended to account for multiple reflections of the spin-flux [61-63]. Hence, although we have verified the device operation with Slonczewski expression [60, 64], the results in this work are based on multi-reflection model and thus the STT efficiency  $\eta_{i>j}$  for spin-flux from layer  $i$  to  $j$  is computed as [63],

$$\eta_{i>2} = -\eta_{2>1} = \frac{P - P\xi\cos(\theta)}{1 - \xi^2\cos^2(\theta)}, \text{ where } \xi = 1 - 2\varepsilon + 2\varepsilon^2 \text{ and } \varepsilon = \frac{1-P}{2} \quad (8)$$

Hence, DLT with linear dependence on  $V_{\text{MTJ}}$  and FLT with the quadratic dependence on  $V_{\text{MTJ}}$  are respectively obtained as,

$$a_{\parallel}^i = \frac{\hbar}{2e} \frac{\eta_{j>i}}{\text{Vol}_{\text{FL}}^i} \frac{V_{\text{MTJ}}}{R_{\text{MTJ}}}, \quad a_{\perp}^i = v \text{abs}(a_{\text{P}}^i) V_{\text{MTJ}} \quad (9)$$

where,  $e$  is the electronic charge and  $v = 2.97/7.82$  is the ratio between the torques extracted from Ref. [55] (for range of values in literature see Table 2.1 and 2.2 of thesis from Kerstin Bernert [65]).

### III. RESULTS and DISCUSSION

#### A. Operation Principle

Figure 1 illustrates the operation principle of the proposed design. For electron flow along  $+z$ -axis, the transmitted spin-flux oriented parallel to  $\mathbf{M}_1$  acts on  $\text{FL}_2$  to attempt to align  $\text{FL}_2$  parallel to  $\text{FL}_1$ , while the reflected spin-flux from  $\text{FL}_2$  which is anti-parallel to  $\mathbf{M}_2$ , attempts to align  $\text{FL}_1$  anti-parallel to  $\text{FL}_2$ . Besides this STT effect, the  $z$ -component of the dipolar-field between both FLs attempts to align them in parallel, while  $x$ -and- $y$  components of the dipolar field which participate in dynamics when FLs are not aligned along  $z$ -axis attempt to align FLs in anti-parallel configuration. Besides these two sets of contentions,

anisotropy field attempts to drive FLs along  $+$  or  $-z$ -axis depending on if  $\mathbf{M}$  is above or below  $x$ - $y$  plane respectively, while demagnetizing field opposes the magnetization vector in respective FLs. For reflected flux to effectuate the switching,  $FL_1$  should be weaker than  $FL_2$ . This means that the critical current for switching  $FL_1$  as free-layer in the traditional pMTJ STT device should be less than the value that would have been obtained for  $FL_2$  as a free-layer. This criterion for the design implies that  $FL_1$  should have weaker PMA (perpendicular anisotropy), i.e. it should be thicker, than  $FL_2$ . For an operational range of the physical and electronic constraints, the above effects enable complete switching of both the FLs successively despite of a unidirectional current, as illustrated in 3D dynamics of the FLs in Fig. 3(a). This is in contrast to traditional STT devices where switching FL into anti-parallel state with respect to (w.r.t) reference layer necessitates a current reversal. The set of  $FL_1$  and  $FL_2$  periodically move across up-up, to down-up, to down-down to up-down state, where up and down refer to magnetization along  $+$  or  $-z$ -axis respectively, which results in resistance switching between parallel and anti-parallel state, as illustrated in Fig. 3(b). When FLs are in up-up state, up-spins act on  $FL_2$  while down-spins act on  $FL_1$ . In this case,  $FL_2$  is receiving spins of the same orientation as its magnetization and hence  $FL_2$  remains unaffected. However for  $FL_1$ , if the current is above the critical current required to switch  $FL_1$  into anti-parallel state, after a certain incubation delay,  $FL_1$  would start to flip to drive pMTJ towards down-up state. In this state,  $FL_1$  receives the spin-flux oriented along the same direction as  $\mathbf{M}_1$  and hence is unaffected. Nevertheless, this transition dynamically starts to change the spin-vector received by  $FL_2$  which now tries to follow switching of  $FL_1$  to align in parallel with it and attempts to drive pMTJ into a down-down state. At the same time, the reflected spin-vector also changes because of the instantaneous change in  $\mathbf{M}_2$  and attempts to push  $FL_1$  to again drive pMTJ into up-down state. These competing effects in asymmetrically designed FLs ensure that FLs flip each other in stable self-sustained oscillations. Note that this

explanation is somewhat oversimplified to enable conceptual understanding of the operation. As can be gauged from the dynamics in Fig. 3(a), the transient magnetization states would rarely be in clear set of up and down states, and mostly would have a significant x and y components thus empowering the contentious effects of the dipolar-coupling to play a significant role in the dynamics. Hence, as evident in Fig. 3(b) one FL starts to switch before another FL is fully switched. The FL dynamics is, however, such that although  $\mathbf{M}_1$  and  $\mathbf{M}_2$  mostly do not exactly align with the z-axis, they do achieve exact parallel and anti-parallel states. This enables the design to achieve full resistance swing from  $R_P$  to  $R_{AP}$  and vice-versa. Note that this design attains theoretical maximum swing, with a constant current input, that can be obtained via STT oscillation, which to the best of our knowledge is not possible even in STNOs with in-plane FL with perpendicular polarizer (pi-Fixed) and perpendicular FL with in-plane reference layer (ip-Fixed) [31, 66-68]. This would be a fundamentally new concept of obtaining oscillations.

These oscillations in resistance electronically translate to the voltage oscillations across a MTJ as shown in Fig. 3(c). The change in  $R_{AP}$  and  $R_{MTJ}$  as the voltage across the MTJ changes is taken into account as earlier noted in the methodology section via eq. (7). FFT of the output  $V_{MTJ}$ , as shown in Fig. 3(d), enables us to obtain the fundamental tone  $f_0$ . A 3 dBm line below the peak value subsequently gives half-power frequencies  $f_1$  and  $f_2$  on either side of  $f_0$ , linewidth  $f_2 - f_1$  and quality-factor (Q) equals  $f_0 / (f_1 - f_2)$ . In Fig. 3(c), an odd observation in this design is the strong amplitude fluctuations for low  $V_{MTJ}$  i.e. when FLs are or nearly parallel to each other. FFT ensures that only the effective swing, which is approximately the visible swing without fluctuations, is computed for  $V_O$ . These fluctuations occur because of the strong dipolar coupling between FLs which tends to lock them together. This assisted with net FLT makes one FL precess around another while DLT tries to align them with damping governed by the damping factor  $\alpha$ . Increasing  $\alpha$ , weakening dipolar field

or weakening FLT reduces this noise, but the oscillator's frequency also reduces. Furthermore, for very high frequency at large currents, i.e. very fast switching, the overlap between dynamics of FL<sub>1</sub> and FL<sub>2</sub> is such that the transient angle between FLs do not reach full 0 and 180 degree, rather the window starts to diminish which degrades the device performance as shown later. To reduce these amplitude fluctuations to improve the output P<sub>O</sub> would be an important future direction implied from these results.

As stated above, there is a physical constraint in pairing of the thickness of the FLs which determines the operability of the design. Therefore, Fig. 4 appraises the effect of FL thickness on device operation to show that design can be optimized to meet frequency spectrum for ASICs and IoT LPWAN over a wide range of specifications. To reiterate, note that for device to work as per our chosen current direction, FL<sub>1</sub> should be weaker (in this case thicker and hence closer to critical thickness at which magnet would become in-plane) than FL<sub>2</sub>, so that FL<sub>1</sub> can switch from the reflected spin-flux. As can be observed from Fig. 4, a smaller difference in the thickness of the two FLs increases the frequency. This however reduces the stability of the oscillations such that they die out as the two thicknesses approach each other. Hence, for smaller difference in the thickness, although frequency increases, the Q of the oscillator and the tunability via current degrades.

## **B. Magnetic Noise**

For the understanding of the operation principle, Fig. 3 and Fig. 4 do not include the effect of the thermal fluctuation field that induces a random phase to the magnetization dynamics [69] of both the FLs and adversely affects the oscillator performance which we discuss now. Thermal fluctuation field results in a Gaussian noise and modelled by eq. (6). It strongly depends on the volume of the magnet Vol<sub>FL</sub>. Effect of this magnetic noise is added in Fig. 5, and all subsequent results, and shows that switching based oscillator is much more

immune to the thermal field than the precessional orbit-based STNO of similar FL volume. Fig. 5(a) shows that both the FLs still switch and oscillate between  $m_z = -1$  and  $+1$ . Nonetheless, the output power  $P_O$  drops by  $-4$  dBm in Fig. 5(b) w.r.t  $P_O$  in Fig. 3(d) without the thermal field. This drop, however, is quite modest compared to what is observed for precessional orbit based STNOs as shown in Fig. 5(c-f). Figure 5(c) and 5(d) illustrate the 3D magnetization dynamics and FFT of  $V_{MTJ}$  for an ip-MTJ based STNO of  $60\text{nm} \times 40\text{nm} \times 4\text{nm}$  ( $1.8\text{nm}$ ) dimensions, with fixed in-plane pinned layer in place of  $FL_1$ . This device can also operate without any external bias field and generate oscillations in the microwave range. Magnetic noise strongly afflicts the orbit as shown in Fig. 5(e) which degrades the  $P_O$  of STNO by  $-15$  dBm in Fig. 5(f). The power gets distributed into the adjacent frequencies which broadens the linewidth and degrades the  $Q$ . In spintronic oscillators, since magnetic noise afflicts the trajectory of the magnetization vector(s), it affects the dynamic angle between FLs thereby affecting the resistance and subsequently  $V_{MTJ}$  oscillations. Therefore, magnetic noise affects both the amplitude noise and the phase noise (quality factor) of the spintronic oscillators. Note that since in this work, switching based design is investigated for only free-running case, we compare with STNO for only free-running case. Injection locking or synchronization of the magnetization dynamics in STNO [14, 15] and phase locking in ring-oscillators [32] dramatically improves their  $Q$ , and may have similar benign effect on the proposed design. This, however, is beyond the scope of the current work and could be a possible future direction to further the investigation of this design. Hence, for the precessional orbit-based designs (free-running case) scaling down the MTJ dimensions has much worse and stronger effect than on switching based design which thus withstands better chances of down-scaling of the magnets.

### C. CCO Configuration

Figure 6 presents oscillator characteristics for a representative dimensions of  $50\text{nm}\times 50\text{nm}\times 1.6\text{nm}(1.2\text{nm})$  for operation in CCO configuration. Here we do not account for the power, area and design of the current sources/mirrors which would drive these oscillators in sync with STNO literature where it is dealt separately [8, 70], and would discuss this issue in the next sub-section. Figure 6(a) shows very large tuning range from 93 MHz to 1002 MHz (red stars) which corresponds to a tuning ratio of 10.77. More detailed comparison of the entire performance metrics is shown in Table I. This is much larger than the values reported for STNOs for current control [31, 66-68] and the ring-oscillators [32]. The output  $V_{\text{MTJ}}$  (blue circles) roll-down from  $-27.5$  dBm at 93 MHz to  $-45$  dBm at 1002 MHz. As the current increases, the voltage drop across MTJ also increases. This reduces  $R_{\text{AP}}$ , the maximum resistance of the MTJ for a given operating bias for the anti-parallel state. Hence, the maximum attainable swing for the resistance oscillations decreases as the voltage increases. This is the reason that despite of the increase in the current,  $V_{\text{MTJ}}$  swing decreases which would have increased had there been no such dependence of the TMR on the voltage bias. Nevertheless, the effectiveness of the proposed design becomes more evident on computing the power consumed (red stars) and the power efficiency (blue circles), illustrated in Fig. 6(b). With an increasing current, as would be expected, the  $P_{\text{IN}}$  increases and the efficiency decreases. Efficiency of 0.12%, i.e. nearly  $-3$  on the logarithmic scale, for STNO [31] corresponds to  $-42$  dBm of output, while for the proposed design at this efficiency corresponds to the output of  $-28$  dBm. Finally, Fig. 6(c) demonstrates that due to the increased noise and the amplitude fluctuations at large currents, and hence at higher frequencies, the linewidth (red stars) increases thereby degrading the Q (blue circles). The Q is in the range of 5.5 to 77.4, while for free-running STNOs good results [31] report in the range of 8 to 39, while again affirms the usefulness of the proposed design.

## D. VCO Configuration

### D.1. Driven by NMOS

An important design consideration often overlooked in spin-oscillator literature is that somehow MTJ needs to be driven by a tunable constant current source which in itself would need a few transistors, and hence comparing MTJ area with a ring oscillator to proclaim area advantage for former is not correct. More than the wide tuning range of VCO/CCO, it becomes more difficult to design stable and widely tunable current sources/mirrors especially at smaller CMOS nodes [8, 70]. Hence, we consider the case of driving MTJ with a single gate-controlled NMOS. Figure 7 illustrates the effect of transition from CCO to gate-controlled VCO configuration. Now, the supply voltage  $V_{DD}$  and the gate voltage are fixed whereas the node connecting MTJ with the drain end of the NMOS is floating. The voltage at this node is now the output voltage  $V_O$  that would be routed to the subsequent stages driven by the oscillator, hence in VCO configuration we compute  $P_O$  corresponding to  $V_O$  instead of  $V_{MTJ}$ . Note that the oscillatory or the ac component of  $V_O$  is just inverted w.r.t ac component of the  $V_{MTJ}$ , and they are different only w.r.t. dc operating point. Hence, to have a proper comparison of the voltage oscillations between VCO and CCO configuration,  $V_O$  in Fig. 7 for a constant current source is inverted by subtracting  $V_{MTJ}$  from 1.1 V which is the  $V_{DD}$  used for the VCO configuration in Fig. 7. Figure 7(a, b) show the  $R_{MTJ}$  and  $V_O$  for CCO configuration for comparison with VCO configuration operating at nearly same frequency (0.7% difference observed in fundamental tone obtained from FFT) by operating CCO configuration at the current equal to the average current observed for the VCO configuration. As the resistance of the MTJ oscillates, it changes the quiescent or the dc operating point of the drain end of the NMOS. Therefore, not only the voltage across MTJ oscillates the current through the cell also oscillates, as shown in Fig. 7(c), in anti-phase with  $R_{MTJ}$  (Fig. 7(d)) i.e. characteristics of the  $I_{MTJ}$  and  $R_{MTJ}$  are inverted w.r.t. each other, while  $V_O$  (Fig. 7(e))

oscillates in-phase with the  $R_{MTJ}$ . The anti-phase oscillations diminish the output voltage swing, which is approximately given by the expression in Fig. 7, mathematically implicit from taking partial derivate of  $V_{MTJ}=I_{MTJ} R_{MTJ}$  with proper phase for all three terms. In the expression,  $I_{AVG}$  is the average of the oscillating current  $I_{MTJ}$  through the cell,  $R_{AVG}$  is the average resistance of the oscillating  $R_{MTJ}$ , and  $\Delta I$  and  $\Delta R$  are the respective swings in current and resistance oscillations. This shows that on driving the proposed oscillator with a NMOS, instead of a current source, the output power  $P_O$  degrades. Results for the comprehensive analysis of this configuration are next presented in Fig. 8. Note that although explicit analysis has not been done for traditional STNO driven by a NMOS like for the proposed design, given the same concept applicable at the drain node for STNO in series with NMOS, we expect similar drop in  $P_O$  for STNO case as well in the same configuration.

## D.2. $V_{GS}$ and $V_{DD}$ Control

In Fig. 8(b-d), tuning of  $V_{DD}$  is shown, which is the mechanism to tune ring-oscillator based VCOs, while Fig. 8(f-h) show that superior characteristics like larger  $P_O$  and power efficiency  $P_O/P_{IN}$  can be obtained for same frequency range by tuning gate voltage  $V_{GS}$  of the NMOS. For both gate and  $V_{DD}$  control, the current increases with the voltage which increases the oscillation frequency (see red stars). However, it is also observed that frequency linearly increases on tuning  $V_{DD}$ , while it saturates for large  $V_{GS}$ . This can be understood from standard textbook approach [71] of the load-line analysis of the system, which is a graphical aid for obtaining the dc bias or the quiescent point of the solution, as shown in Fig. 8(a, e, i). Load-line analysis gives the dc current through NMOS and the dc voltage at the drain terminal. In the following discussion for simplicity we momentarily consider  $R_{MTJ}$  as a constant, a trivial resistor. As shown in Fig. 8(e), for gate-control with fixed  $V_{DD}$ , the output characteristics of the NMOS i.e. current  $I_{DS}$  vs. drain-to-source voltage  $V_{DS}$  characteristic for

an increasing gate-to-source voltage  $V_{GS}$  is intersected with a single line of the output characteristic of a resistor which intercepts the y-axis at  $V_{DD}/R_{MTJ}$  and x-axis at  $V_{DD}$  and has a slope of  $-1/R_{MTJ}$ . This shows that although the current increases with the increasing  $V_{GS}$ , the drain voltage or the operating  $V_{DS}$  obtained at the intersection point (red dots) reduces. Now, contrast it with the solution for  $V_{DD}$  control for a fixed gate voltage shown in Fig. 8(a). This would now have a single line (actually superimposed, with larger  $V_{DD}$  line overshadowing the smaller  $V_{DD}$  trend line) for NMOS output characteristic, while multiple parallel lines for  $R_{MTJ}$  of  $-1/R_{MTJ}$  slope, one each for increasing supply voltage  $V_{DD}$ . For this case, now both the current and the operating  $V_{DS}$  obtained at the intersection point increases. For  $V_{DD}$  control thus notice that if the quiescent point (red dots) enter the saturation region of the transistor, the current has almost no change (slightly increase due to non-saturating behaviour at smaller nodes due to the short-channel effects), while  $V_{DS}$  would continue to increase. If, however, quiescent point is in the triode region, both  $I_{DS}$  and  $V_{DS}$  would increase continuously. Whereas for the gate-control with quiescent point in the triode region, as  $V_{GS}$  increases both the decrease in the operational  $V_{DS}$  and the increase in the  $I_{DS}$  start to saturate. Because of the large  $R_{MTJ}$  and the large current requirements to switch the FLs, the voltage drop across MTJ forces the transistor to operate in the triode region in this work. Hence, it is because of this operating or the dc bias of the system with NMOS in the triode region, and the current  $I_{DS}$  and drain voltage  $V_{DS}$  following the explanation above, the frequency continuously increases for  $V_{DD}$  control while it saturates for the gate-control of the oscillator. Thereafter, observe that in VCO configuration the lowest frequency operable is lower than that in CCO configuration (see Table I for explicit numbers). This is because the current  $I_{DS}$  also oscillate in the VCO configuration. At the lowest frequency in the VCO configuration, despite of the average drain current  $I_{AVG}$  being lower than the value at which the oscillator would have operated because of the current oscillations for a substantial fraction of the time-

period the current is much larger than the lowest operating current in the CCO configuration. This current drive is sufficient to trigger the oscillator. The downside of these current oscillations is to degrade the  $P_O$ , as noted earlier and illustrated in Fig. 7.  $P_O$  (blue circles in Fig. 8(b, f)), however not only degrades it also exhibits more complex behaviour in the VCO configuration which we attempt to understand by again going back to expression in Fig. 7. This can be understood abstractly as follows. The increasing trend of  $P_O$  is observed when increase in the current outdo the fall in MTJ resistance due to latter's dependence on the TMR, while a decreasing trend of  $P_O$  is observed just like for CCO configuration when increase in current is insufficient to compensate for the decrease in  $R_{MTJ}$ . Now, we expound the more detailed mechanism. As explained for the frequency trend, the current increases for both type of controls, and thus  $I_{AVG}$  increases in both cases. Because of the dependence of TMR on  $V_{MTJ}$ ,  $R_{AP}$  and hence  $\Delta R$  and  $R_{AVG}$  reduce as the current increases in both cases. The quiescent point of the drain terminal now acts as an additional constraint for regulating potential drop across the MTJ and hence constraints  $\Delta R$  and  $R_{AVG}$ . As a result, for  $V_{DD}$  control,  $\Delta R \cdot I_{AVG}$  first increases and then decreases whereas for gate-control it always decreases and starts to saturate. The non-linear dependence of the current on the respective voltage control and the non-linear relation between  $R_{MTJ}$  and the  $V_{MTJ}$ , however results in firstly an increasing and then decreasing trend for  $\Delta I$  (current oscillations) for the  $V_{DD}$  control while mainly an increasing trend for the gate-control. Putting  $R_{AVG}$  and  $\Delta I$  together, for both  $V_{DD}$  and gate-control,  $R_{AVG} \cdot \Delta I$  continuously decreases with an increasing control voltage. Hence,  $R_{AVG}$ ,  $\Delta I$ ,  $\Delta R$  and  $I_{AVG}$  collude to result in  $V_O$  or  $P_O$  trend observed in Fig. 8(b, f). Besides the trends observe that gate-control enables larger  $P_O$  because of the full-scale  $V_{DD}$  which equals to the node supply voltage, whereas lower  $V_{DD}$  due to the  $V_{DD}$ -control for the oscillator inherently limits the  $V_O$  and the  $P_O$ . Here note that irrespective of the control, one shortcoming of this design w.r.t. ring-oscillator (see Table I) used for ASIC clocks, however,

is still the formers much lower output power which implies that an additional amplifier driven by  $V_O$  signal may still be needed and consume additional area and energy. The design of this amplifier is however is beyond the purview of the current work and hence the configurations in Table I for each column are prudently specified to bring out this difference explicitly to notice.

Next, the power consumed  $P_{IN}$  (red stars) in Fig. 8(c, g), as expected, follows the same trend as the current or the frequency for respective type of voltage controls. Larger  $P_O$  for the gate-control, with  $P_{IN}$  in the same range as for  $V_{DD}$ -control, evidently results in a larger power-efficiency  $P_O/P_{IN}$  (blue circles) for the gate-control. Furthermore, note that for the gate-control, the cell does not load the preceding driving stage or the circuit which generate the control voltage because of the large (theoretically infinite) input impedance of the gate terminal of the transistor, while for the  $V_{DD}$ -control much smaller the drain-to-source impedance, w.r.t. gate input impedance, loads the driving circuit. Therefore for practical designs, we suggest gate-control of the oscillator instead of following the  $V_{DD}$ -control method of the ring-oscillators. The linewidth, and the inferred quality factor, extracted from the FFT follow even more complex behaviour. Besides magnetic noise which has Gaussian random distribution, the complexity is enhanced due to the amplitude noise generated when  $R_{MTJ}$  tends to  $R_P$  (see Fig. 3(c)). As explained in the operation mechanism, when the two FLs become nearly parallel, one FL starts to strongly precess around another and results in rapid oscillations. These two random factors add to the previous circuit analysis propounded for the frequency and  $P_O$  trends. As a result, it is more meaningful to look at the overall trend instead of the exact points for the linewidth and the quality factor in Fig. 8(d, h). Overall it is observed that linewidth (red stars) and quality-factor (blue circles) are best for mid-range control voltage for both  $V_{DD}$  and  $V_{GS}$  control, and degrade as the drive current because of the control voltage is either reduced or increased. At the larger frequencies at the larger currents,

as previously noted in the operation mechanism, the dynamic angle  $\theta$  between FLs does not reach full 0 and 180 degree and starts to diminish. Alternatively, it can be understood as an increasing overlap between the transient characteristic of the  $m_z$  of the two FLs or the asymmetric phase shift in the transients. More simply, larger currents trigger faster switching of the two FLs which are affected asymmetrically because of their asymmetric design (different thickness for the same ferromagnetic parameters). This not only slightly reduces the  $V_O$ , it also increases the importance of the traditional precessional trajectories and concurrently increases the fraction of time per cycle spent by one FL to precess around another when they are nearly parallel. For relatively lower currents, the ability to achieve exact parallel and anti-parallel states had considerably reduced the torques that act on FLs to destabilize them for the alignment. The increased weightage or the importance of the precession thus increases the importance or the influence of the magnetic noise on the oscillations, which results in the increased linewidth and the reduced quality factor. On the other hand, for decreasing voltage for very weak currents tending towards critical current requirement for the switching of each FL, firstly as expected the incubation time for the onset of the oscillations increases (not shown). Secondly, the current starts to become insufficient to see this delay in the oscillations from period-to-period, i.e. the switching is slow enough to have FLs in perfect parallel and anti-parallel states with both  $\mathbf{M}_1$  and  $\mathbf{M}_2$  aligned along z-axis long enough, rendering the torques to near zero such that the following effects play a significant role. The role of dipolar-field becomes important to unlock from these conditions, especially when the FLs are in anti-parallel configuration. But more importantly, it is the dependence on the random thermal-field which increases to unlock from these alignments and the key cause of the period-to-period variations from the oscillations between  $R_P$  and  $R_{AP}$  states, since the random thermal-fields would introduce random angle-offsets in  $\theta$  making one switching cycle faster than the other. Therefore, the linewidth increases and the quality factor

decreases for very weak currents. Observe that the same physics is also illustrated in Fig. 6(c) for the CCO operation where linewidth increases for the small currents. The Q factor, computed as  $f_0/(f_1-f_2)$  i.e. the ratio of fundamental tone to the linewidth, thus follows the simultaneous effect on the fundamental frequency and the linewidth for both CCO and the VCO configurations. Hence, at both ends of the current strength, the linewidth is large and the quality factor is small. The Q is in the range of 3 to 39.4, which is lower than the values obtained in CCO configuration, but still comparable to the free-running STNOs good results [31] which report in the range of 8 to 39. The VCO frequency is now in the range of 85 MHz to 420 MHz, which limits its applicability to ASIC clocks, the tunability ratio of 4.92. This ratio is still much greater than both for STNO and ring-oscillators (see Table I). These results show that even in the VCO configuration with a single NMOS, the proposed design can contest with the effectiveness of the other oscillator designs.

### D.3. MTJ Area

Figure 8(i-l) next appraises the effect of scaling MTJ cross-section for a fixed drive strength of the NMOS. Figure 8(i) is the load-line analysis for a fixed NMOS with fixed  $V_{DD}$  and  $V_{GS}$ , while the area of the MTJ is scaled which proportionately scales  $R_{MTJ}$  because of a constant RA-product. In Fig. 8(j), the oscillator frequency goes down with the increasing area because the current density scales down almost quadratically with the MTJ dimension. Deviation from the quadratic trend happens because of the changes in the dc bias conditions (red dots in Fig. 8(i)) due to the change in  $R_{MTJ}$ . As the  $R_{MTJ}$  scales-down for the fixed operating condition of the NMOS, the drain current and the dc voltage of the drain terminal increases while dc bias across MTJ i.e. approximately the average value of  $V_{MTJ}$  reduces. This increase in the current, however, cannot over-ride the decrease in the current density due to the quadratic effect of the scaling-up of the MTJ dimension. Hence, the frequency (red

stars) scales-down but the trend is weaker than the trend that would have been obtained for pure quadratic effect of area scaling. Fixed RA product also results in scaling down of both  $\Delta R$  and  $R_{AVG}$  which is again weaker because of the smaller dc value of  $V_{MTJ}$  due to the shift in the bias conditions. The shifts in the bias conditions also allow for much more steep increase in  $I_{AVG}$  than in  $\Delta I$ . This is further assisted positively by an increased thermal stability of the MTJ because magnetic noise is directly proportional to the square-root of the volume of the magnet. Because of these three reasons, the output power  $P_O$  (blue circles) increases with increasing cross-section but at the cost of the frequency. Increase in the current also results in increase in  $P_{IN}$  (red stars) as shown in Fig. 8(k), but the improvement in  $P_O$  still results in a higher power-efficiency (blue circles) for the larger MTJ cross-sections. Furthermore, as expected from the effect of the volume of the magnet on the magnetic noise, the linewidth and the quality factor improve, i.e. linewidth (red stars) reduces and  $Q$  (blue circles) increases, as the MTJ cross-section increases in Fig. 8(l). Observe that for 40-50% increase in the dimension from 50 nm to 70-75 nm or nearly twice the increase in the area of the MTJ,  $Q$  has increased by nearly three times from 26 to 85. This shows that if for a given frequency the design permits the use of a larger MTJ, it could be extremely advantageous in terms of the output power, power-efficiency and the quality factor. To examine this viability, we next appraise the scaling of the drive strength of the NMOS across three CMOS nodes and understand how they provide us the margin for using larger MTJs despite of scaling-down of the CMOS nodes.

#### **D.4. NMOS W/L Scaling**

In Fig. 9, the effect of scaling channel width of NMOS to its length, i.e. W/L ratio, for 14 nm, 65 nm and 130 nm CMOS node is studied, integrated with MTJ of dimensions  $50\text{nm} \times 50\text{nm} \times 1.6\text{nm}$  (1.2nm) i.e. cross-sectional area of  $0.0025 \mu\text{m}^2$ . As expected the average

current  $I_{AVG}$  for all three nodes increases with the increasing W/L in Fig. 9(a), and almost saturates because of the integration of the NMOS with the MTJ resistor which determines the dc bias of the system. The channel area is computed as explained in the methodology section and illustrated for reference in Fig. 9(b). Y-axis is on the log-scale for the better representation of the data. Channel area increases with the increase in the channel width. For 14 nm node, channel-area is from  $0.00168 \mu\text{m}^2$  to  $0.0468 \mu\text{m}^2$ , for 65 nm node it is from  $0.009245 \mu\text{m}^2$  to  $0.194 \mu\text{m}^2$ , and for 130 nm node from  $0.0245 \mu\text{m}^2$  to  $0.5145 \mu\text{m}^2$  for W/L ratio from 5 to 105 respectively. From Fig. 9(a, c) we observe that for 14 nm node,  $I_{AVG}$  is from  $168 \mu\text{A}$  at 102.5 MHz to  $289 \mu\text{A}$  at 248.5 MHz, for 65 nm node it is from  $178 \mu\text{A}$  at 110.12 MHz to  $511 \mu\text{A}$  at 518 MHz, and for 130 nm node from  $339 \mu\text{A}$  at 292 MHz to  $633 \mu\text{A}$  at 656 MHz for W/L ratio from 5 to 105 respectively. Note that from this data we do not compute tunability ratio because channel width is not normally electronically tunable in the VCO or CCO design. We would however come back to this point at the end of this section to re-examine this constraint. The node supply-voltage  $V_{DD}$  is 0.7 V, 1.1 V and 1.3 V respectively for the three nodes. Hence, it can be observed from the data that MTJ is always smaller than the channel area of the NMOS, except for 14 nm node at W/L=5, channel-area for W/L=10 at 14 nm node is  $0.002646 \mu\text{m}^2$ . Furthermore, channel-area of the NMOS is smaller than the actual area of the NMOS which includes the area for the drain and the source region. This shows that firstly design area would be dominated by the transistor instead of the MTJ and thus should serve as the rightful parameter for comparing area with other designs like ring oscillators. This fact has often been ignored in STNO literature and the power and area of the driving unit has been ignored as well while comparing the designs. Secondly, within the periphery of the folded (because of the large W/L) NMOS, larger MTJ can be used without any additional penalty on the design area. Therefore, this W/L analysis for the NMOS over three CMOS nodes shows the viability of using larger MTJs to boost the

performance of the oscillator. These results also show that MTJ technology does not need to directly scale-down or at least at the same pace with the CMOS technology for the proposed oscillator. Next, the comparison across nodes in Fig. 9(d) shows that using larger nodes for the oscillator design would be beneficial as the nominal supply voltage of the node also scales down with it thereby reducing the drive capability of the transistors. Unfortunately, the data also implies that scaling-down the CMOS node limits the operational range of the oscillator and for a given current (iso-frequency) degrades the output and consumes more channel area, for instance compare approximately between the last point of 14 nm and the second point of 65 nm trends.

#### **D.5. DCO Configuration**

Finally, we re-examine the comment on the electronic control of the channel widths. Since the W/L analysis shows that a large channel width for bulk-NMOS or a large numbers of fins for FinFETs are required to operate this design, it provides the ability to extend the VCO based analog design to a coarse DCO based digital design, as illustrated in Fig. 10. For an N-bit digital control from  $D_0$  to  $D_{N-1}$  which corresponds to digital input from 1 to  $2^N-1$ , the width or the number of fins can be discretized across multiple transistors in parallel (wire-ORed i.e. drain terminal tied together) driving a common MTJ. The effective width of the transistor corresponding to a more significant bit ‘m’ would be twice the width or twice the number of fins of the transistor corresponding to the adjacent less significant bit ‘m-1’. In the DCO design, the gate terminal receives full scale voltage as logic 1 and the transistor is turned-off for logic 0 on receiving 0 V input, hence magnitudes of both its  $V_{GS}$  and  $V_{DD}$  are fixed. This scheme enables an electronic control of the effective channel width or an effective transistor whose channel-width directly corresponds to the digital input. The lowest digital input of 1 obtained by setting only lowest significant bit to logic 1 and others to logic 0 would

correspond to the lowest targeted frequency of the oscillator, while the input  $2^N - 1$  obtained by setting all of the N-bits to logic 1 state would correspond to the largest targeted frequency, where the ratio of the largest to the lowest frequency would give us the tunability ratio for the DCO.

#### IV. SUMMARY

We propose a fundamentally new concept of obtaining oscillations with frequencies in VHF and UHF bands. We posit a novel scheme of the spin-torque oscillators which is based on the superior full-switching of the free-layers in contrast to the extant precessional orbit-based schemes. Moreover, it is shown that the free-layers can be reversibly switched without reversing the direction of the current. Oscillator is shown to operate without any external magnetic field and any pinned layer. Absence of the need of a pinning layer may in fact result in a smaller stack height and integration of the oscillator in a lower metallic layers in contrast to a standard MTJs which are pushed to higher layers because of a thick stack-size. The oscillator is shown to operate in the range of 85 MHz to 1002 MHz, with the tuning ratio of 10.76 (CCO) and 4.92 (VCO), output from  $-26$  to  $-47$  dBm. The analysis including the driving NMOS shows that they dominate the design area and the larger nodes would be better for driving the proposed oscillator. Moreover, because of the dominance of the transistor on the area, the scaling constraints on the MTJ can be relatively relaxed, and the oscillator performance can be further improved compared to results generally presented in this work. Table I illustrates some of our exemplar results (second and third column) against other oscillators in the literature. It shows that our design may indeed enable very large tuning-range, with good Q factor, very small area for a decent output signal and power-efficiency, which is much superior to especially STNO, in the frequency range useful for ASIC clocks and long-range low-power IoT communication via LoRa protocol.

## Corresponding Authors

†gauravdce07@gmail.com \*elelg@nus.edu.sg

## ACKNOWLEDGEMENTS

This work at the National University of Singapore was supported by CRP award no. NRF-CRP12-2013-01 and MOE2013-T2-2-125. We gratefully acknowledge the discussions with Xuanyao Fong, the useful review comments on the manuscript from Kien Trinh Quang and Sachin for helping with Fig. 1.

## References

- [1] L. Dai, R. Harjani, Design of High-Performance CMOS Voltage-Controlled Oscillators, in: The Springer International Series in Engineering and Computer Science, Analog Circuits and Signal Processing, Springer US,, Boston, MA, 2003.
- [2] C.C. Chung, W.S. Su, C.K. Lo, A 0.52/1 V Fast Lock-in ADPLL for Supporting Dynamic Voltage and Frequency Scaling, IEEE Transactions on Very Large Scale Integration (VLSI) Systems 24, 408-412 (2016).
- [3] J.v.d. Tang, D. Kasperkovitz, A.H.M.v. Roermund, High-frequency oscillator design for integrated transceivers, in, Kluwer Academic Publishers, Boston, 2003.
- [4] A. Jha, K. Liao, G. Yeap, K.O. Kenneth, Voltage controlled oscillator area reduction in nano-scale CMOS, in: 2014 IEEE Radio Frequency Integrated Circuits Symposium, 2014, pp. 421-424.
- [5] T. Chen, R.K. Dumas, A. Eklund, P.K. Muduli, A. Houshang, A.A. Awad, D. P. x00Fc, rrenfeld, B.G. Malm, A. Rusu, J, x00C, kerman, Spin-Torque and Spin-Hall Nano-Oscillators, Proceedings of the IEEE 104, 1919-1945 (2016).
- [6] T. Chen, A. Eklund, S. Sani, S. Rodriguez, B.G. Malm, J. Åkerman, A. Rusu, Integration of GMR-based spin torque oscillators and CMOS circuitry, Solid-State Electronics 111, 91-99 (2015).
- [7] H.S. Choi, S.Y. Kang, S.J. Cho, I.-Y. Oh, M. Shin, H. Park, C. Jang, B.-C. Min, S.-I. Kim, S.-Y. Park, C.S. Park, Spin nano-oscillator-based wireless communication, Scientific Reports 4, 5486 (2014).
- [8] T. Chen, P. Dürrenfeld, S. Rodriguez, J. Åkerman, A. Rusu, A highly tunable microwave oscillator based on MTJ STO technology, Microwave and Optical Technology Letters 56, 2092-2095 (2014).
- [9] T. Moriyama, G. Finocchio, M. Carpentieri, B. Azzerton, D.C. Ralph, R.A. Buhrman, Phase locking and frequency doubling in spin-transfer-torque oscillators with two coupled free layers, Physical Review B 86, 060411 (2012).
- [10] X. Zhu, J.G. Zhu, Bias-Field-Free Microwave Oscillator Driven by Perpendicularly Polarized Spin Current, IEEE Transactions on Magnetics 42, 2670-2672 (2006).
- [11] D.E. Nikonov, G.I. Bourianoff, Spin torque oscillator having multiple fixed ferromagnetic layers or multiple free ferromagnetic layers, US8604886 B2, Google Patents, 2016.
- [12] H. Ryo, K. Hitoshi, T. Sumito, T. Shingo, Y. Kay, F. Akio, M. Rie, I. Hiroshi, Y. Shinji, Magnetic field angle dependence of out-of-plane precession in spin torque oscillators having an in-plane magnetized free layer and a perpendicularly magnetized reference layer, Applied Physics Express 9, 053006 (2016).
- [13] C.H. Sim, M. Moneck, T. Liew, J.-G. Zhu, Frequency-tunable perpendicular spin torque oscillator, Journal of Applied Physics 111, 07C914 (2012).
- [14] T. Nagasawa, K. Kudo, H. Suto, K. Mizushima, R. Sato, Large-amplitude, narrow-linewidth microwave emission in a dual free-layer MgO spin-torque oscillator, Applied Physics Letters 105, 182406 (2014).
- [15] M. Al-Mahdawi, Y. Toda, Y. Shiokawa, M. Sahashi, Low-nonlinearity spin-torque oscillations driven by ferromagnetic nanocontacts, Physical Review B 93, 024408 (2016).
- [16] P.M. Braganca, K. Pi, R. Zakai, J.R. Childress, B.A. Gurney, Zero field high frequency oscillations in dual free layer spin torque oscillators, Applied Physics Letters 103, 232407 (2013).
- [17] S. Witold, S. Tomasz, W. Jerzy, R. Günter, D. Sebastiaan van, Zero-Field Spin Torque Oscillator Based on Magnetic Tunnel Junctions with a Tilted CoFeB Free Layer, Applied Physics Express 5, 063005 (2012).

- [18] M. Hiroki, K. Hitoshi, S. Yoshishige, S. Takayuki, N. Kazumasa, N. Yoshinori, T. Koji, F. Akio, A. Hiroko, T. Tomohiro, I. Hiroshi, A. Koji, Y. Shinji, High Q factor over 3000 due to out-of-plane precession in nano-contact spin-torque oscillator based on magnetic tunnel junctions, *Applied Physics Express* 7, 023003 (2014).
- [19] H. Arai, R. Matsumoto, S. Yuasa, H. Imamura, Spin-Torque Induced Oscillation of a Magnetoresistive Nanopillar with a Conically Magnetized Free Layer and an In-Plane Magnetized Reference Layer, *Journal of the Physical Society of Japan* 85, 063802 (2016).
- [20] L. Bianchini, S. Cornelissen, J.-V. Kim, T. Devolder, W. van Roy, L. Lagae, C. Chappert, Direct experimental measurement of phase-amplitude coupling in spin torque oscillators, *Applied Physics Letters* 97, 032502 (2010).
- [21] Z. Zeng, P.K. Amiri, I.N. Krivorotov, H. Zhao, G. Finocchio, J.-P. Wang, J.A. Katine, Y. Huai, J. Langer, K. Galatsis, K.L. Wang, H. Jiang, High-Power Coherent Microwave Emission from Magnetic Tunnel Junction Nano-oscillators with Perpendicular Anisotropy, *ACS Nano* 6, 6115-6121 (2012).
- [22] R. Giordano, A. Aloisio, F. Ameli, V. Bocci, S. Cadeddu, V. Izzo, A. Lai, S. Mastroianni, Performance of a high-frequency synthesizable digitally-controlled oscillator, in: 2014 IEEE Nuclear Science Symposium and Medical Imaging Conference (NSS/MIC), 2014, pp. 1-2.
- [23] C. Zhiqing, Z. Qi, W. Ning, Y. Dunshan, L. Guohong, W. Hui, F. Songlin, A low spur CMOS phase-locked loop with wide tuning range for CMOS Image Sensor, in: ASIC (ASICON), 2013 IEEE 10th International Conference on, 2013, pp. 1-4.
- [24] Y. Li, L. Liu, X. Huang, R. Zhang, R. Li, Design and ASIC Implementation of High-Speed DDC, in: Digital Manufacturing and Automation (ICDMA), 2011 Second International Conference on, 2011, pp. 365-368.
- [25] Z. Zhang, Y. Zhiyi, C. Xu, Z. Xiaoyang, A low power 1.0 GHz VCO in 65nm-CMOS LP-process, in: ASIC (ASICON), 2011 IEEE 9th International Conference on, 2011, pp. 1006-1009.
- [26] X. Deng, J. Yang, J. Wu, Low jitter ADPLL insensitive to power supply noise, in: Industrial Technology (ICIT), 2010 IEEE International Conference on, 2010, pp. 1050-1054.
- [27] Semtech, LoRaWAN Specification v1.0, (January 2015).
- [28] J. Pet, rvi, K. Mikhaylov, H. M. inen, J. Inatti, Evaluation of LoRa LPWAN technology for remote health and wellbeing monitoring, in: 2016 10th International Symposium on Medical Information and Communication Technology (ISMICT), 2016, pp. 1-5.
- [29] J. So, D. Kim, H. Kim, H. Lee, S. Park, LoRaCloud: LoRa platform on OpenStack, in: 2016 IEEE NetSoft Conference and Workshops (NetSoft), 2016, pp. 431-434.
- [30] J.P. Bardyn, T. Melly, O. Seller, N. Sornin, IoT: The era of LPWAN is starting now, in: ESSCIRC Conference 2016: 42nd European Solid-State Circuits Conference, 2016, pp. 25-30.
- [31] Z. Zeng, G. Finocchio, B. Zhang, P.K. Amiri, J.A. Katine, I.N. Krivorotov, Y. Huai, J. Langer, B. Azzerboni, K.L. Wang, H. Jiang, Ultralow-current-density and bias-field-free spin-transfer nano-oscillator, *Scientific Reports* 3, 1426 (2013).
- [32] H. Gao, L. Sun, X. Kuang, L. Lou, A low-phase-noise ring oscillator with coarse and fine tuning in a standard CMOS process, *Journal of Semiconductors* 33, 075004 (2012).
- [33] S. Tyagi, M. Alavi, R. Bigwood, T. Bramblett, J. Brandenburg, W. Chen, B. Crew, M. Hussein, P. Jacob, C. Kenyon, C. Lo, B. McIntyre, Z. Ma, P. Moon, P. Nguyen, L. Rumaner, R. Schweinfurth, S. Sivakumar, M. Stettler, S. Thompson, B. Tufts, J. Xu, S. Yang, M. Bohr, A 130 nm generation logic technology featuring 70 nm transistors, dual Vt transistors and 6 layers of Cu interconnects, in: Electron Devices Meeting, 2000. IEDM '00. Technical Digest. International, 2000, pp. 567-570.
- [34] Z. Luo, A. Steegen, M. Eller, R. Mann, C. Baiocco, P. Nguyen, L. Kim, M. Hoinkis, V. Ku, V. Klee, F. Jamin, P. Wrschka, P. Shafer, W. Lin, S. Fang, A. Ajmera, W. Tan, D. Park, R. Mo, J. Lian, D. Vietzke, C. Coppock, A. Vayshenker, T. Hook, V. Chan, K. Kim, A. Cowley, S. Kim, E. Kaltalioglu, B. Zhang, S. Marokkey, Y. Lin, K. Lee, H. Zhu, M. Weybright, R. Rengarajan, J. Ku, T. Schiml, J. Sudijono, I. Yang, C. Wann, High performance and low power transistors integrated in 65nm bulk CMOS technology, in: Electron Devices Meeting, 2004. IEDM Technical Digest. IEEE International, 2004, pp. 661-664.
- [35] S. Natarajan, M. Agostinelli, S. Akbar, M. Bost, A. Bowonder, V. Chikarmane, S. Chouksey, A. Dasgupta, K. Fischer, Q. Fu, T. Ghani, M. Giles, S. Govindaraju, R. Grover, W. Han, D. Hanken, E. Haralson, M. Haran, M. Heckscher, R. Heussner, P. Jain, R. James, R. Jhaveri, I. Jin, H. Kam, E. Karl, C. Kenyon, M. Liu, Y. Luo, R. Mehandru, S. Morarka, L. Neiberg, P. Packan, A. Paliwal, C. Parker, P. Patel, R. Patel, C. Pelto, L. Pipes, P. Plekhanov, M. Prince, S. Rajamani, J. Sandford, B. Sell, S. Sivakumar, P. Smith, B. Song, K. Tone, T. Troeger, J. Wiedemer, M. Yang, K. Zhang, A 14nm Logic Technology Featuring 2nd-Generation FinFET , Air-Gapped Interconnects, Self-Aligned Double Patterning and a 0.0588 m2 SRAM cell size, in: 2014 IEEE International Electron Devices Meeting, 2014, pp. 3.7.1-3.7.3.

- [36] D.V. Berkov, N.L. Gorn, Numerical Simulation of Quasistatic and Dynamic Remagnetization Processes with Special Applications to Thin Films and Nanoparticles, in: Y. Liu, D.J. Sellmyer, D. Shindo (Eds.) Handbook of Advanced Magnetic Materials, Springer US, Boston, MA, 2006, pp. 794-880.
- [37] Z. Li, S. Zhang, Magnetization dynamics with a spin-transfer torque, *Physical Review B* 68, 024404 (2003).
- [38] A. Jaiswal, X. Fong, K. Roy, Comprehensive Scaling Analysis of Current Induced Switching in Magnetic Memories Based on In-Plane and Perpendicular Anisotropies, *IEEE Journal on Emerging and Selected Topics in Circuits and Systems* 6, 120-133 (2016).
- [39] Y. Zhou, H. Zhang, Y. Liu, J. Åkerman, Macrospin and micromagnetic studies of tilted polarizer spin-torque nano-oscillators, *Journal of Applied Physics* 112, 063903 (2012).
- [40] G.S. Kar, W. Kim, T. Tahmasebi, J. Swerts, S. Mertens, N. Heylen, T. Min, Co/Ni based p-MTJ stack for sub-20nm high density stand alone and high performance embedded memory application, in: 2014 IEEE International Electron Devices Meeting, 2014, pp. 19.11.11-19.11.14.
- [41] A.A. Timopheev, R. Sousa, M. Chshiev, L.D. Buda-Prejbeanu, B. Dieny, Respective influence of in-plane and out-of-plane spin-transfer torques in magnetization switching of perpendicular magnetic tunnel junctions, *Physical Review B* 92, 104430 (2015).
- [42] S. Ikeda, K. Miura, H. Yamamoto, K. Mizunuma, H.D. Gan, M. Endo, S. Kanai, J. Hayakawa, F. Matsukura, H. Ohno, A perpendicular-anisotropy CoFeB–MgO magnetic tunnel junction, *Nat Mater* 9, 721-724 (2010).
- [43] R. Engel-Herbert, T. Hesjedal, Calculation of the magnetic stray field of a uniaxial magnetic domain, *Journal of Applied Physics* 97, 074504 (2005).
- [44] N. Kani, S.C. Chang, S. Dutta, A. Naeemi, A Model Study of an Error-Free Magnetization Reversal Through Dipolar Coupling in a Two-Magnet System, *IEEE Transactions on Magnetics* 52, 1-12 (2016).
- [45] A. Aharoni, Demagnetizing factors for rectangular ferromagnetic prisms, *Journal of Applied Physics* 83, 3432-3434 (1998).
- [46] K. Roy, S. Bandyopadhyay, J. Atulasimha, K. Munira, A.W. Ghosh, Energy dissipation and switching delay in spin-transfer torque switching of nanomagnets with low-saturation magnetization in the presence of thermal fluctuations, arxiv:1107.0387 (2011).
- [47] H. Keiji, N. Makoto, U. Tomomasa, A. Hisanori, I. Sumio, A. Yoshiaki, Y. Hiroaki, N. Akihiro, Effect of Self-Heating on Time-Dependent Dielectric Breakdown in Ultrathin MgO Magnetic Tunnel Junctions for Spin Torque Transfer Switching Magnetic Random Access Memory, *Japanese Journal of Applied Physics* 49, 04DD15 (2010).
- [48] C. Chul-Min, O. Young-Taek, K. Kyung-Jun, P. Jin-Suk, S. Hiroaki, M. Seiji, K. Sung-Kyu, L. Jeong-Yong, S. Yun-Heub, Temperature dependence of reliability characteristics for magnetic tunnel junctions with a thin MgO dielectric film, *Semiconductor Science and Technology* 31, 075004 (2016).
- [49] B. Oliver, G. Tuttle, Q. He, X. Tang, J. Nowak, Two breakdown mechanisms in ultrathin alumina barrier magnetic tunnel junctions, *Journal of Applied Physics* 95, 1315-1322 (2004).
- [50] C. Yoshida, M. Kurasawa, Y.M. Lee, K. Tsunoda, M. Aoki, Y. Sugiyama, A study of dielectric breakdown mechanism in CoFeB/MgO/CoFeB magnetic tunnel junction, in: 2009 IEEE International Reliability Physics Symposium, 2009, pp. 139-142.
- [51] D.V. Dimitrov, Z. Gao, X. Wang, W. Jung, X. Lou, O.G. Heinonen, Dielectric breakdown of MgO magnetic tunnel junctions, *Applied Physics Letters* 94, 123110 (2009).
- [52] S. Amara-Dababi, R.C. Sousa, M. Chshiev, H. Béa, J. Alvarez-Hérault, L. Lombard, I.L. Prejbeanu, K. Mackay, B. Dieny, Charge trapping-detrapping mechanism of barrier breakdown in MgO magnetic tunnel junctions, *Applied Physics Letters* 99, 083501 (2011).
- [53] Y. Lu, M. Tran, H. Jaffrès, P. Seneor, C. Deranlot, F. Petroff, J.M. George, B. Lépine, S. Ababou, G. Jézéquel, Spin-Polarized Inelastic Tunneling through Insulating Barriers, *Physical Review Letters* 102, 176801 (2009).
- [54] Z. Kugler, V. Drewello, M. Schäfers, J. Schmalhorst, G. Reiss, A. Thomas, Temperature and bias voltage dependence of Co/Pd multilayer-based magnetic tunnel junctions with perpendicular magnetic anisotropy, *Journal of Magnetism and Magnetic Materials* 323, 198-201 (2011).
- [55] H. Kubota, A. Fukushima, K. Yakushiji, T. Nagahama, S. Yuasa, K. Ando, H. Maehara, Y. Nagamine, K. Tsunekawa, D.D. Djayaprawira, N. Watanabe, Y. Suzuki, Quantitative measurement of voltage dependence of spin-transfer torque in MgO-based magnetic tunnel junctions, *Nat Phys* 4, 37-41 (2008).
- [56] J.C. Sankey, Y.-T. Cui, J.Z. Sun, J.C. Slonczewski, R.A. Buhrman, D.C. Ralph, Measurement of the spin-transfer-torque vector in magnetic tunnel junctions, *Nat Phys* 4, 67-71 (2008).
- [57] K. Takahide, D. Tadaomi, O. Mikihiro, A. Yasuo, M. Terunobu, Tunneling Spin Polarization and Magnetic Properties of Co–Fe–B Alloys and Their Dependence on Boron Content, *Japanese Journal of Applied Physics* 46, L250 (2007).

- [58] S.X. Huang, T.Y. Chen, C.L. Chien, Spin polarization of amorphous CoFeB determined by point-contact Andreev reflection, *Applied Physics Letters* 92, 242509 (2008).
- [59] J.C. Slonczewski, Current-driven excitation of magnetic multilayers, *Journal of Magnetism and Magnetic Materials* 159, L1-L7 (1996).
- [60] J.C. Slonczewski, Currents, torques, and polarization factors in magnetic tunnel junctions, *Physical Review B* 71, 024411 (2005).
- [61] X. Waintal, E.B. Myers, P.W. Brouwer, D.C. Ralph, Role of spin-dependent interface scattering in generating current-induced torques in magnetic multilayers, *Physical Review B* 62, 12317-12327 (2000).
- [62] S. Hernández, R.H. Victora, Calculation of spin transfer torque in partially polarized spin valves including multiple reflections, *Applied Physics Letters* 97, 062506 (2010).
- [63] W. Zhu, Z. Zhang, J. Zhang, Y. Liu, Multiple Reflection Effect on Spin-Transfer Torque Dynamics in Spin Valves with a Single or Dual Polarizer, *SPIN* 05, 1550003 (2015).
- [64] T. Tomohiro, A. Hiroko, T. Sumito, T. Shingo, K. Hitoshi, I. Hiroshi, Critical Field of Spin Torque Oscillator with Perpendicularly Magnetized Free Layer, *Applied Physics Express* 6, 123003 (2013).
- [65] K. Bernert, Spin-transfer torques in MgO-based magnetic tunnel junctions, Doctoral Thesis, Technische Universität Dresden (2014).
- [66] D. Houssameddine, U. Ebels, B. Delaet, B. Rodmacq, I. Firastrau, F. Ponthenier, M. Brunet, C. Thirion, J.P. Michel, L. Prejbeanu-Buda, M.C. Cyrille, O. Redon, B. Dieny, Spin-torque oscillator using a perpendicular polarizer and a planar free layer, *Nat Mater* 6, 447-453 (2007).
- [67] O. Boulle, V. Cros, J. Grollier, L.G. Pereira, C. Deranlot, F. Petroff, G. Faini, J. Barnas, A. Fert, Shaped angular dependence of the spin-transfer torque and microwave generation without magnetic field, *Nat Phys* 3, 492-497 (2007).
- [68] F. Ciarán, S. Volker, B. Kerstin, L. Jürgen, F. Jürgen, H.R. William, R.P. Matthew, E.R. Stephen, M.D. Alina, Zero-field spin-transfer oscillators combining in-plane and out-of-plane magnetized layers, *Applied Physics Express* 7, 043001 (2014).
- [69] W.F. Brown, Thermal Fluctuations of a Single-Domain Particle, *Physical Review* 130, 1677-1686 (1963).
- [70] T. Chen, Wideband amplifier design for STO technology, Master's thesis, KTH Royal Institute of Technology, Integrated Devices and Circuits, (2011).
- [71] A.S. Sedra, K.C. Smith, *Microelectronic Circuits*, Oxford University Press, 2004.

## Figures

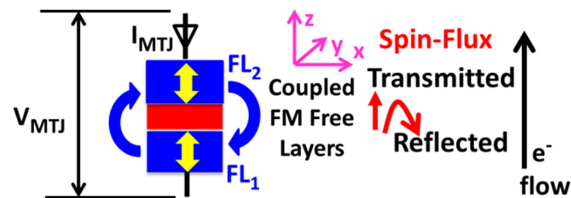


**Figure 1.** Conceptual illustration of a pMTJ with a dipolar coupled dual free-layer, without any pinned layer. It is driven by a uni-directional current from FL<sub>2</sub> to FL<sub>1</sub>. The transmitted spin-flux with vector parallel to the magnetization of FL<sub>1</sub> acts on FL<sub>2</sub>, while reflected spin-flux with vector anti-parallel to magnetization of FL<sub>2</sub> acts on FL<sub>1</sub>, which for a set of electronic and geometric constraints results in a self-sustained switching of both the free layers producing ac oscillations for a dc bias. When this pMTJ is driven via tunable dc current source  $I_{MTJ}$  device is in CCO configuration.

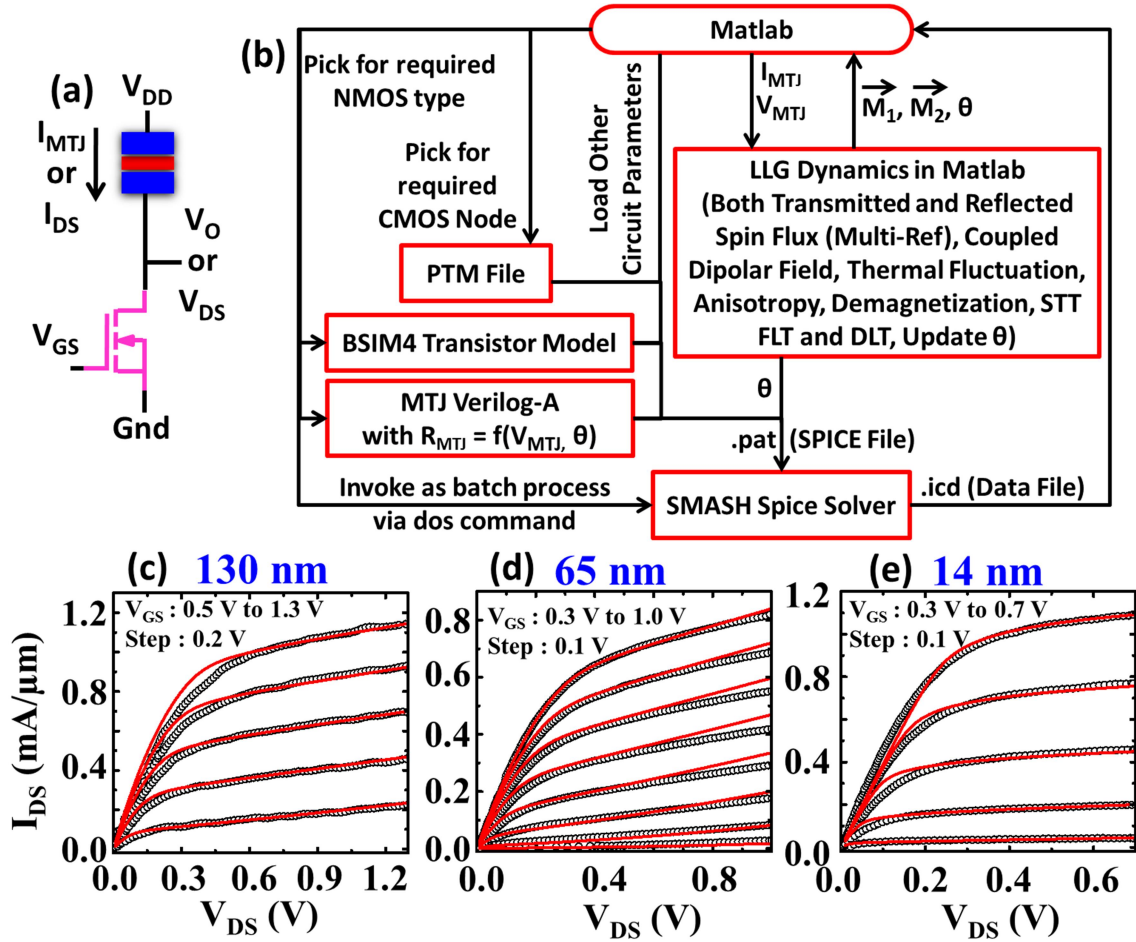


**Figure 2.** (a) VCO configuration with pMTJ driven via tunable dc  $V_{GS}$  for a fixed  $V_{DD}$  (gate-control) or tunable dc  $V_{DD}$  for a fixed  $V_{GS}$  (drain-control). (b) Schematic summary of simulation framework expounded in the methodology section. (c-e) Published experimental data (black circles) of NMOS output characteristics fitted (red line) against BSIM4 model used in spice solver for three representative CMOS nodes. For (c) 130 nm node fitting against Fig. 4 of Ref. [33] from Intel, (d) 65 nm node fitting against Fig. 6 of Ref. [34] from IBM, Chartered and Infineon, and (e) 14 nm node fitting against Fig. 5 of Ref. [35] from Intel.

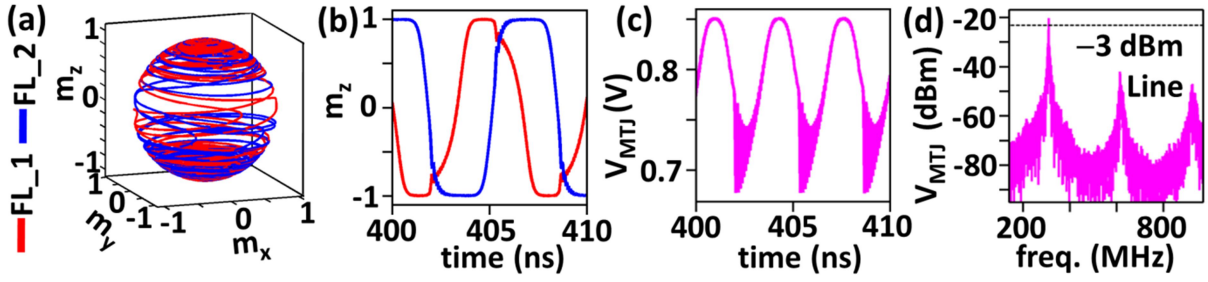


**Figure 3.** Operation principle (without thermal field) for  $50\text{nm}\times 50\text{nm}\times 1.6\text{nm}(1.2\text{nm})$  pMTJ device driven with constant current  $I_0$  of  $360\ \mu\text{A}$ . (a) Dynamics of magnetization unit vector  $\mathbf{m} = [m_x\ m_y\ m_z]$ . (b) Full-switching of both  $m_z$ . (c) Output voltage oscillations  $V_{\text{MTJ}}$  and (d) FFT of  $V_{\text{MTJ}}$  demonstrating fundamental tone and the harmonics along with  $-3\text{dBm}$  line used to determine the linewidth of the oscillator.

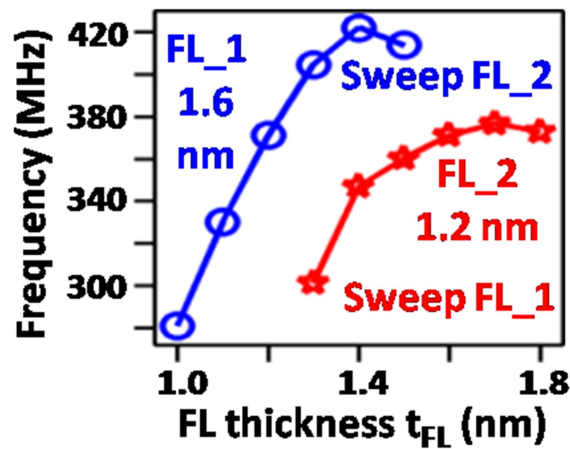


**Figure 4.** Effect of FL thickness (without thermal field) on the oscillation frequency for a representative  $I_0$  of  $410\ \mu\text{A}$ . MTJ can thus be designed to meet frequency specifications of an oscillator over a wide frequency range.

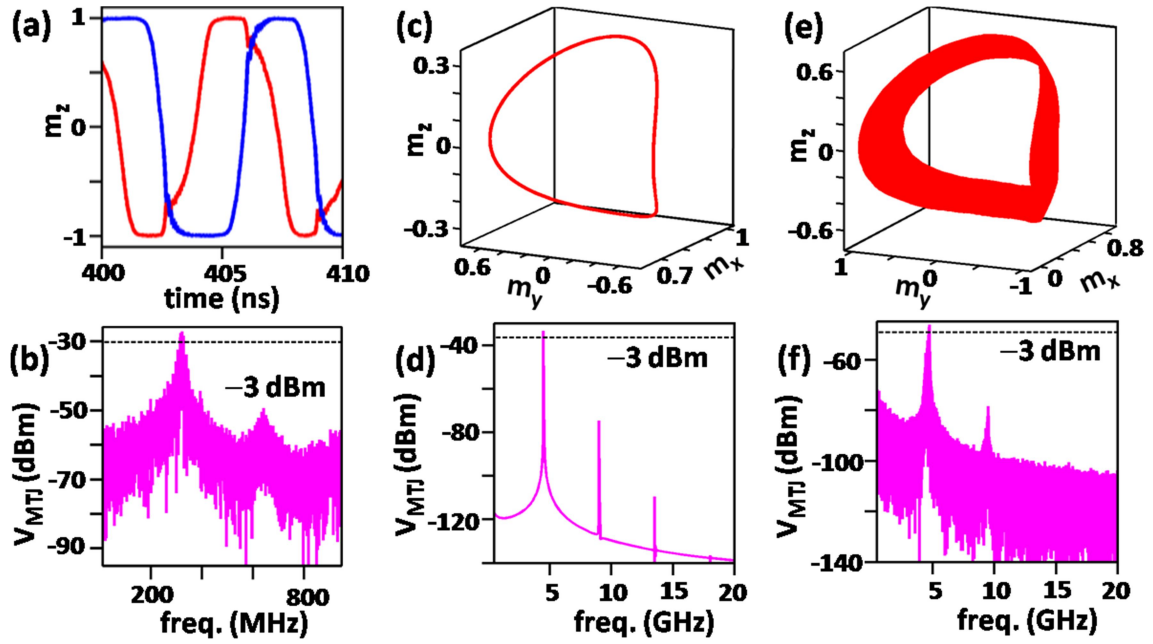


**Figure 5.** Effect of the thermal fluctuation field or magnetic noise (300 K) on the proposed oscillator (a, b) is contrasted with an orthogonal STNO (c-f), of same RA-product, of  $60\text{nm}\times 40\text{nm}\times 4\text{nm}(1.8\text{nm})$  with in-plane fixed layer (in place of  $\text{FL}_1$ ) and perpendicular free layer (in place of  $\text{FL}_2$ ) operating at 4.5 GHz with  $70\ \mu\text{A}$  fixed current without external bias field. (c, d) STNO without thermal field clearly shows the precessional orbit (c) and FFT of the voltage across MTJ (d). (e-f) STNO with thermal field shows randomness introduced in the orbit ((e) illustration represents only 50 ns of precession), and the linewidth broadening in FFT in (f). Proposed design is shown to be robust to thermal field with minor effect ( $-4\ \text{dBm}$  calculated from obtained points) on output and increase in the linewidth, while STNO of comparable cross-section and FL thickness shows strong degradation ( $-15\ \text{dBm}$ ) of output and phenomenal change in the linewidth.

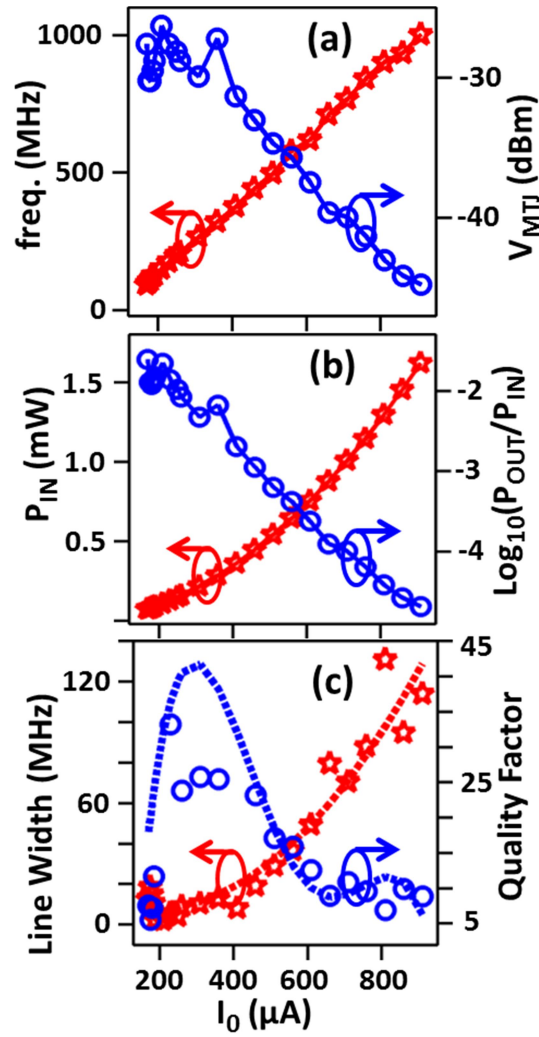


**Figure 6.** Effect of constant current  $I_0$  on (a) frequency and output voltage oscillations, (b) input power consumed  $P_{IN}$  and the power efficiency ( $P_{OUT}/P_{IN}$ ) i.e. delivered output power to the consumed power, (c) linewidth and the quality factor ( $Q$ ) of the oscillator. (b) Consumed power decreases directly with the current thereby improving the power efficiency especially at the lower frequencies. (c) Frequency spectra narrows at the smaller currents (frequencies) thereby improving the quality factor from 10 to nearly 30.

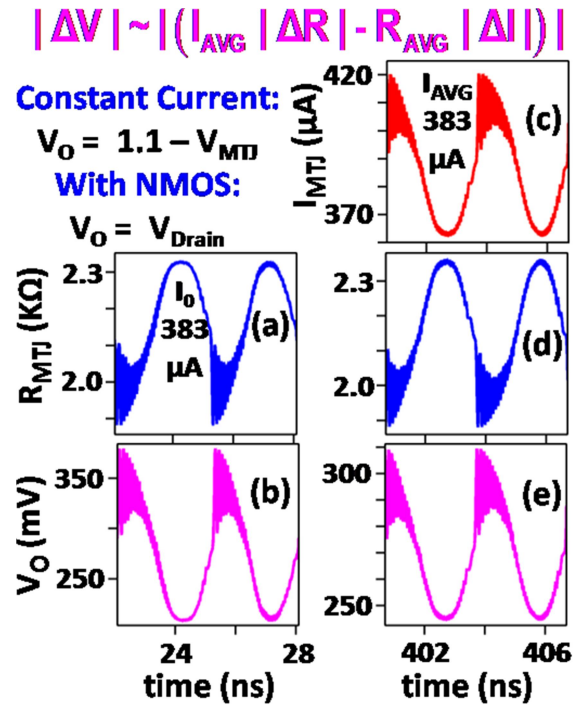


**Figure. 7.** Effect of replacing constant current drive (a, b) with NMOS (c-e) (65 nm Node, W/L=15,  $V_{DD}=V_{GS}=1.1V$ ) to drive MTJ. With NMOS, drain current also oscillates in anti-phase with resistance, thereby reducing the output swing which is approximately given by expression on top of the figure.  $I_0$  is chosen equal to the average drain current, and complementary MTJ voltage is used as  $V_O$  for constant current case, for rightful comparison.

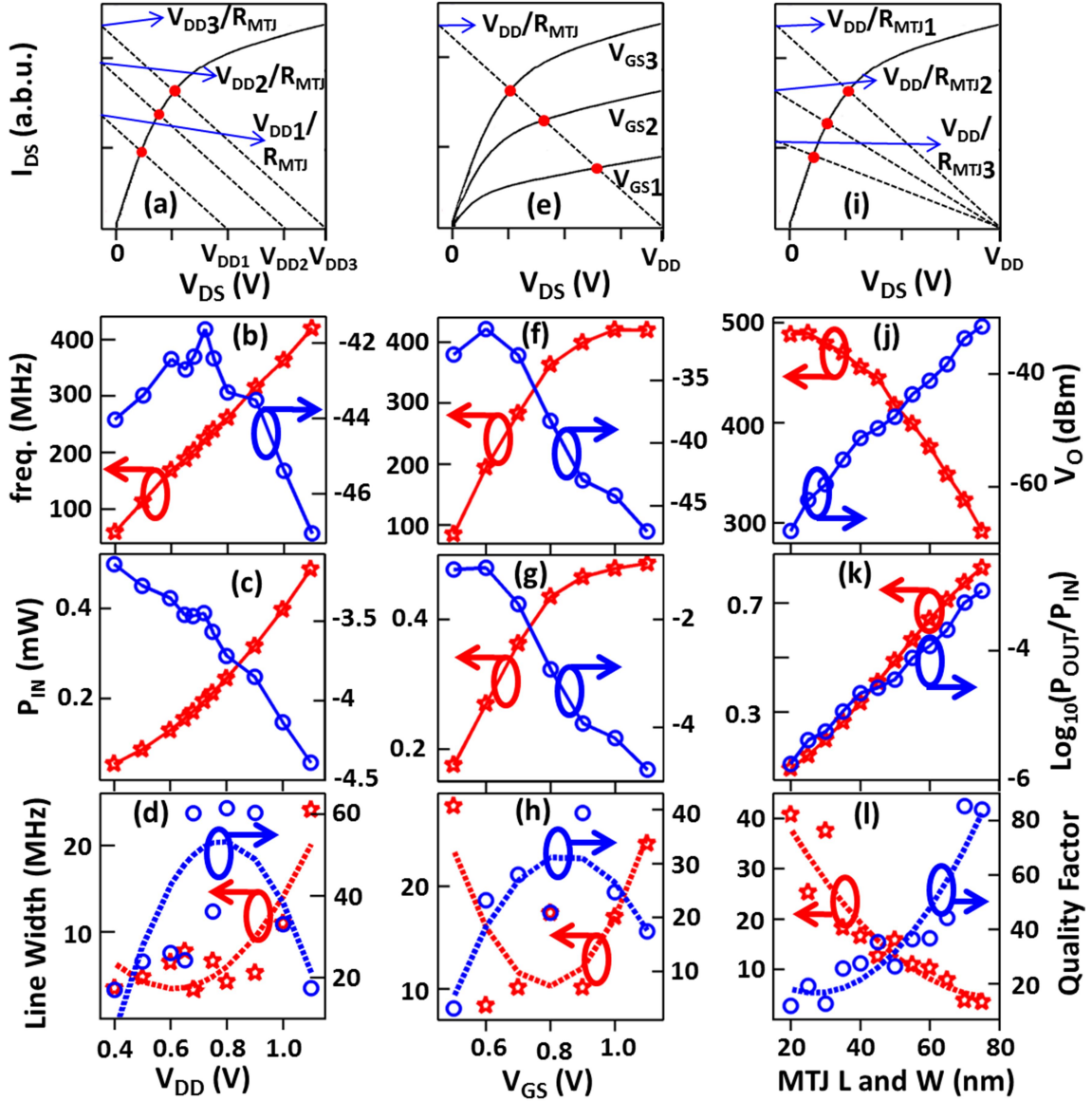


**Figure 8.** Effect of sweeping (a-d) drain voltage (akin to the ring oscillators), (e-h) gate voltage (suggested for this oscillator), and (i-l) MTJ cross-section (length=width). (a, e, i) Conceptual illustration (see section D for details) of load-line analysis to show the effect of sweeping  $V_{DD}$ ,  $V_{GS}$  and MTJ cross-section in respective column, with larger index in the subscript representing a larger magnitude of the corresponding quantity. Solid black line is NMOS output characteristics. Dashed black line is  $R_{MTJ}$  output characteristic, where  $R_{MTJ}$  is treated as a constant trivial resistor in (a), (e) and (i). Quiescent point is marked via red dot at the point of intersection of  $R_{MTJ}$  and NMOS characteristics. This serves as an aid in understanding data in respective columns. (b-d, f-h, j-l) NMOS is chosen for 65 nm CMOS

node with  $W/L=25$ , while for (b-d, f-h) MTJ dimensions are  $50\text{nm}\times 50\text{nm}\times 1.6\text{nm}$  ( $1.2\text{nm}$ ) and for (j-l)  $V_{DD}=V_{GS}=1.1\text{ V}$ . Observe that for the larger cross-section, MTJs have very high  $Q$ , high efficiency and large  $V_O$  because of the large volume which gives more immunity to the thermal fluctuation field, but lower frequency because of smaller current density.

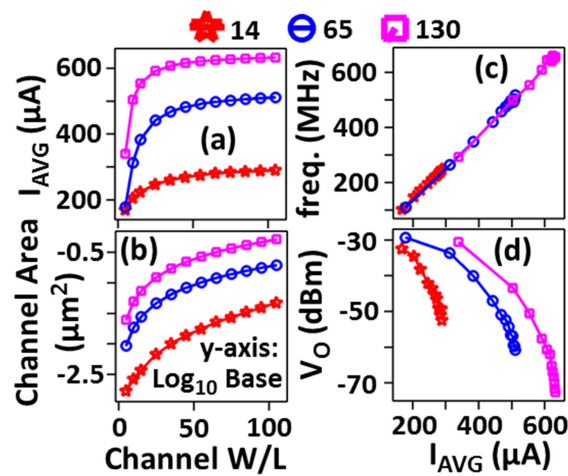


**Figure 9.** Effect of  $W/L$  of transistors on performance across 14 nm, 65 nm and 130 nm node operating at full scale node voltage (0.7, 1.1, 1.3 V) i.e.  $V_{DD}=V_{GS}$ . (a) Average operating current for the oscillator. (b) Channel area for the reference. Output frequency (c) and the signal amplitude (d).

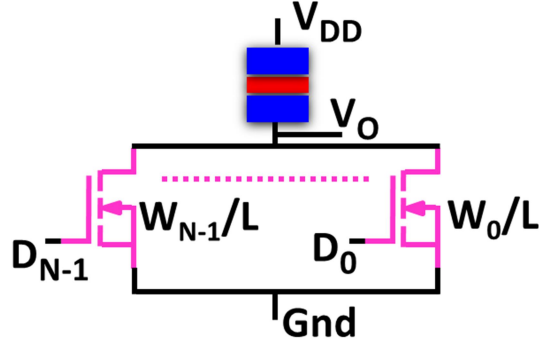


**Figure 10.** Re-designing VCO into a DCO configuration by splitting the effective transistor width across wire-ORed N-transistors, driven by N-bit digital control  $D_0$  to  $D_{N-1}$ . Effective width for bulk-NMOS or number of fins for FinFET of transistor ‘m’, driven by bit  $D_m$ , is twice the width or number of fins of transistor ‘m-1’ where  $m \in [1, N-1]$ .

Table I. Summary of a comparison with other designs in the literature.

Criteria	pp 9 (C)	pp 9, $\beta$ (NMOS)	STNO $\kappa, \chi, \delta$ (pi/ip) (C)	Ring $\lambda, \zeta$ [32]
Freq. (f) (MHz)	93 – 1002	85 - 420	600 – 4000 [31, 66-68]	480-1100
$f_{\max}/f_{\min}$	10.77	4.92	~ 2 &	1.25
$V_O$ (dBm)	-26 to -45	-31 to -47	-42 &	-2.97
$P_O/P_{IN}$ (%)	2.5 to 0.002	0.3 to 0.004	0.12 &	13.1
Q	5.5 - 77.4	3 – 39.4	8-39 &	-120 to -108 dBc/Hz $\Phi$
Area ( $\mu\text{m}^2$ )	0.0025 *	0.0462 #	0.0105 * &	14784 $\Psi$

C: Driven by Current Source; \* MTJ area; # Channel Area;  $\Psi$  Core Area;

9.  $50 \times 50 \times 1.6(1.2)$ ;  $\beta$ . Gate Control 65 Node  $W/L=25$ ;  $\delta$ .  $50 \times 40 \times t_1(t_2)$ ;  $\kappa$ . ii and pp need external B-Field to precesses.  $\chi$ . TMR Based without additional locking or post-processing circuit;  $\delta$  See Table 1 of Ref. [31]; & Best of the results of Ref. [31];  $\lambda$  LC is not compared, because in sub-GHz range on-chip inductor and capacitor size is in hundreds of  $\mu\text{m}^2$ . Its comparison is better suited in high GHz range.  $\Phi$  Phase Noise (not Q);  $\zeta$  with PLL lock (not for free-running case).